processes

MDPI

Article

Enhancing the Photocatalytic Performance of $BiVO_4$ for Micropollutant Degradation by Fe and Ag Photomodification

Marin Popović [1], Tayebeh Sharifi [2,3], Marijana Kraljić Roković [2], Boštjan Genorio [4], Boštjan Žener [4], Igor Peternel [1], Urška Lavrenčič Štangar [4], Hrvoje Kušić [2,5,*], Ana Lončarić Božić [2] and Marin Kovačić [2,*]

[1] Department of Safety and Protection, Karlovac University of Applied Sciences, Trg Josipa Juraja Strossmayera 9, HR-47000 Karlovac, Croatia; m210p90@gmail.com (M.P.); ipeternel@vuka.hr (I.P.)
[2] Faculty of Chemical Engineering and Technology, University of Zagreb, Trg Marka Marulića 19, HR-10000 Zagreb, Croatia; tayebeh.sharifi@ijs.si (T.S.); mkralj@fkit.unizg.hr (M.K.R.); abozic@fkit.unizg.hr (A.L.B.)
[3] Jožef Stefan Institute, Jamova cesta 39, SI-1000 Ljubljana, Slovenia
[4] Faculty of Chemistry and Chemical Technology, University of Ljubljana, Večna pot 113, SI-1000 Ljubljana, Slovenia; bostjan.genorio@fkkt.uni-lj.si (B.G.); bostjan.zener@fkkt.uni-lj.si (B.Ž.); urska.lavrencic.stangar@fkkt.uni-lj.si (U.L.Š.)
[5] University Center Koprivnica, University North, Trg dr. Žarka Dolinara 1, HR-48000 Koprivnica, Croatia
* Correspondence: hkusic@fkit.unizg.hr (H.K.); mkovacic@fkit.unizg.hr (M.K.); Tel.: +385-1-4597-160 (H.K.); +385-1-4597-145 (M.K.)

Abstract: Wider application of $BiVO_4$ (BVO) for photocatalytic water treatment is primarily limited by its modest photocatalytic effectiveness, despite its appropriately narrow band gap for low-cost, sunlight-facilitated water treatment processes. In this study, we have photomodified an isotype BVO, consisting of a tetragonal zircon and monoclinic scheelite phase, with Fe (Fe@BVO) and Ag (Ag@BVO) ionic precursors under UV illumination in an aqueous ethanol solution in order to assess their effect on the opto-electronic properties and effectiveness for the removal of ciprofloxacin (CIP). Fe@BVO failed to demonstrate enhanced effectiveness over pristine BVO, whereas all Ag@BVO achieved improved CIP degradation, especially 1% Ag@BVO. At pH 4 and 6, 1% Ag@BVO demonstrated nearly 24% greater removal of CIP than BVO alone. Photomodification with Fe created surface oxygen vacancies, as confirmed by XPS and Mott–Schottky analysis, which facilitated improved electron mobility, although no distinct Fe-containing phase nor Fe-doping was detected. On the other hand, the introduction of mid-band gap states by oxygen vacancies decreased the reducing power of the photogenerated electrons as the flat band potentials were shifted to more positive values, thus likely negatively impacting superoxide formation. In contrast, Ag-photomodification (Ag@BVO) resulted in the formation of Ag_2O/AgO and Ag nanoparticles on the surface of BVO, which, under illumination, generated hot electrons by surface plasmon resonance and enhanced the mobility of photogenerated electrons. Our research underscores the pivotal role of photogenerated electrons for CIP degradation by $BiVO_4$-based materials and emphasizes the importance of appropriate band-edge engineering for optimizing contaminant degradation.

Keywords: $BiVO_4$; ciprofloxacin; design of experiments; isotype homojunction; modification; iron; silver; photomodification; vacancy

Citation: Popović, M.; Sharifi, T.; Kraljić Roković, M.; Genorio, B.; Žener, B.; Peternel, I.; Lavrenčič Štangar, U.; Kušić, H.; Lončarić Božić, A.; Kovačić, M. Enhancing the Photocatalytic Performance of $BiVO_4$ for Micropollutant Degradation by Fe and Ag Photomodification. *Processes* **2023**, *11*, 2803. https://doi.org/10.3390/pr11092803

Academic Editors: Vesna Tomašić, Andrea Petrella and Antoni Sanchez

Received: 31 July 2023
Revised: 3 September 2023
Accepted: 19 September 2023
Published: 21 September 2023

1. Introduction

Bismuth vanadate ($BiVO_4$) is a non-toxic, chemically stable, n-type visible light photocatalyst that has shown promise in various environmental applications due to its favorable properties [1–3]. Due to its favorable band gap of 2.4 eV, which facilitates the use of the solar spectrum, suitable band edge positions, and good stability under illumination $BiVO_4$, is often investigated for photoelectrochemical water splitting and environmental remediation, either alone or as part of Z-schemes and composite photocatalysts [4–9]. Its inherent photocatalytic performance depends on several parameters: the polymorph in question, particle

size, and specific surface area [1,10,11]. $BiVO_4$ is known to have three crystal polymorphs: two tetragonal forms, zirconia and scheelite analogues, and a monoclinic modification with a distorted scheelite structure. The monoclinic polymorph exhibits superior photocatalytic activity to the individual tetragonal polymorphs [3,12,13], and its efficacy in degrading organic dyes has been well-established [3]. Nonetheless, specific modifications to further enhance the effectiveness of $BiVO_4$ are necessary, as even the monoclinic polymorph suffers from high recombination rates and low charge carrier mobility [14,15]. Therefore, strategies to further enhance the photocatalytic properties of photocatalysts, including $BiVO_4$, are doping, the formation of composites, introduction of a cocatalyst, morphological and crystalline modifications, the creation of novel nanostructures, and surface engineering [16–18]. Doping and composite formation with other photocatalysts are the most common approaches, while photodeposition of cocatalysts, although not as common, holds substantial promise.

Cocatalysts aim to reduce the band gap of the formed composite, improving the optical response of the photocatalytic material and suppressing the recombination rate of photogenerated charges by sinking photogenerated charges (i.e., holes and/or electrons), and, in turn, maximizing the surface population of charge carriers on the newly formed composite photocatalyst [17,19–21]. In photodeposition, the procedure utilizes the photogenerated charges formed by the photocatalyst itself. For example, holes can oxidize transition metal complexes, leading to the deposition of their respective oxides on the surface of the photocatalyst, while electrons can reduce ionic species into their respective nanometals [22].

Herein, we have attempted to modify an isotype homojunction $BiVO_4$ consisting of a tetragonal and monoclinic phase, the synthesis and properties of which we have reported earlier [23,24], with iron and silver species using a photomodification procedure akin to photodeposition. To the best of our knowledge, this work represents the first time such a modification of an isotype homojunction $BiVO_4$ has been reported. Aqueous silver ions can be reduced to silver nanoparticles (AgNPs) on the surface of $BiVO_4$, which could facilitate the inhibition of photogenerated charge recombination due to the formation of a Schottky barrier, increase light absorption in the visible range due to surface plasmon resonance (SPR), and generate hot electrons that can form superoxide radicals [25–30]. We hypothesize that photomodification with Fe^{2+} can induce defect states in the band structure of $BiVO_4$, which can facilitate the inhibition of photogenerated charge recombination inhibition and modulate the band gap structure of $BiVO_4$. In addition, Fe^{2+} can undergo oxidation to form iron oxide species on the surface of $BiVO_4$, leading to the formation of a Z-scheme and improving photocatalytic performance [31]. Furthermore, as part of this work, we have attempted to modify the iso-type homojunction $BiVO_4$ materials without an inert atmosphere, in a medium consisting of 20:80 *v*:*v* ethanol–water. The photocatalytic performance of the obtained materials was investigated for the degradation of ciprofloxacin (CIP), a synthetic antibiotic used to treat respiratory, urinary, and skin infections in humans and animals, as a model organic pollutant. In the environment, CIP adversely affects the development and reproduction of several aquatic organisms and contributes to the proliferation of antibiotic resistant pathogens [32,33]. The novel insights into the effects of Ag and Fe photomodification on iso-type homojunction $BiVO_4$ presented herein pave the way to a broader application of iso-type homojunction $BiVO_4$ and contributes to the knowledge on $BiVO_4$ band structure engineering.

2. Materials and Methods

2.1. Synthesis of $BiVO_4$ and Photomodification of Ag and Fe Species

$BiVO_4$ was prepared by a co-precipitation method as described in previous work [34]. In brief, bismuth(III) nitrate pentahydrate ($Bi(NO_3)_3 \times 5H_2O$, VWR Chemicals, Lutterworth, UK), ammonium metavanadate (NH_4VO_3, Acros Organics, Geel, Belgium), ethylenediaminetetraacetic acid disodium salt dihydrate (EDTA-2Na, T.T.T., Sveta Nedjelja, Croatia), and nitric acid (HNO_3, Lach-ner, Neratovice, Czech Republic) were used. First, solutions of

0.2 M bismuth(III) nitrate and 0.2 M ammonium metavanadate were prepared by dissolving the required amounts in 1.5 M nitric acid (HNO_3, Lach-ner, Neratovice, Czech Republic) with stirring at 80 °C. For the preparation of the stock nitric acid solution, ultra-pure water was used, which was sourced from a DirectQ-3 UV (Merck Millipore, Burlington, MA, USA). Then, an appropriate amount of Na-EDTA was added to obtain a concentration of 0.02 M Na-EDTA in the aforementioned Bi^{3+} precursor solution. The precursor solutions were quantitatively combined in a 1:1 v/v ratio and were allowed to stir for one week at room temperature in the dark. $BiVO_4$ was separated from the reaction solution by centrifugation at 1370× g for 3 min (EBA 21, Andreas Hettich GmbH, Tuttlingen, Germany). The precipitate was washed with ultrapure water three times and centrifuged consecutively. The $BiVO_4$ slurry obtained after final washing was dried at 80 °C until dry in a natural convection laboratory oven (UN-55, Memmert, Schwabach, Germany). The dried product was ground using an agate pestle and mortar and was calcined in air at 450 °C for 2 h in a muffle furnace (LP-08, Instrumentaria, Zagreb, Croatia).

For the photomodification procedure of Ag or Fe species, in order to obtain Ag@BVO and Fe@BVO, silver (I) nitrate ($AgNO_3$, Kemika, Zagreb, Croatia) and iron (III) chloride hexahydrate ($FeCl_3 \times 6H_2O$, Kemika, Zagreb, Croatia) were used, respectively. Photomodification was performed with an intensely mixed dispersion of pristine $BiVO_4$ ($\gamma(BiVO_4)$ = 10,000 mg L^{-1}) in a solution of 20:80 v/v ethanol:water. To this dispersion, an appropriate amount of Ag or Fe precursors was added in order to achieve 1, 8, or 15 wt% Ag or 5, 27.5, or 50 wt% Fe content. The dispersion was placed under intense, unfiltered, and collimated irradiation of a 450 W xenon arc lamp (XBO 450W OFR, Osram, Germany) housed in a research arc lamp housing (Oriel/Newport, Irvine, CA, USA). The lamp was operated in constant power mode with a model 69920 arc lamp power supply (Oriel/Newport, Irvine, CA, USA). After illumination over 60 min, the samples were washed and dried as described previously for pristine $BiVO_4$.

2.2. Preparation of Immobilized $BiVO_4$ Films

Films of pristine $BiVO_4$ (BVO), Fe-modified (Fe@BVO), and Ag-modified (Ag@BVO) $BiVO_4$ on round borosilicate glass plates (r = 37.5 mm) for photocatalytic experiments were obtained by spin-coating a suspension of the photocatalysts dispersed in a titania/silicate sol-gel binder [34]. For this purpose, a titanate precursor sol (TiO_2-sol) was prepared by hydrolyzing titanium isopropoxide ($Ti\{OCH(CH_3)_2\}_4$) in a dilute aqueous solution of ethanol (EtOH, Gram-mol, Zagreb, Croatia, Φ_{EtOH} = 0.026) acidified with perchloric acid ($HClO_4$, Kemika, Zagreb, Croatia, Φ_{HClO4} = 0.021). The sol was hydrolyzed under reflux for 48 h. In addition, a silicate precursor sol (SiO_2-sol) was prepared by hydrolysis of tetraethylorthosilicate (TEOS, $Si\{OC_2H_5\}_4$, Acros Organics, Geel, Belgium) in water acidified with hydrochloric acid (HCl, Kemika, Zagreb, Croatia, Φ_{HCl} = 0.23. The volume fraction of TEOS was ΦTEOS = 0.74. The hydrolysis of TEOS was carried out at room temperature and under vigorous stirring until a clear sol was obtained. The final coating sol was prepared by dispersing 163 g L^{-1} of the respective catalyst in a sol composed of $\Phi_{TiO2\text{-}sol}$ = 0.429 and $\Phi_{SiO2\text{-}sol}$ = 0.061, with the addition of Levasil® 200/30 (Kurt Obermeier, Bad-Berleburg, Germany, $\Phi_{Levasil®\ 200/30}$ = 0.102) and EtOH (Φ_{EtOH} = 0.408). A 750 µL aliquot of the final coating sol was then dropped onto a glass plate that was spun at 1500 rpm for 30 s using a KW-4A spin coater (Chemat Technologies, Northridge, CA, USA). The coated plates were then thermally fixated by heating them to 200 °C for 2 h in an UN-55 laboratory oven (Memmert, Schwabach, Germany).

2.3. Photocatalytic Experiments

The experiments were carried out in a photocatalytic reactor equipped with a water-cooling jacket placed under a collimated beam of simulated solar light passed through an AM1.5 global air mass filter (Oriel/Newport Corporation, Irvine, CA, USA) using the research arc lamp and source outlined in Section 2.1. The volume of the working solution during the experiments was 80 ± 0.5 mL. The pH of the solution was adjusted beforehand

to suit the conditions determined by the statistical experimental planning approach. Full factorial design (FFD) experimental plans, Table S1, were used to simultaneously investigate the effect of the Ag or Fe wt% and pH on the photocatalytic effectiveness for the degradation of ciprofloxacin (CIP) as a model pollutant at a concentration of 50 μM. Designs with three center points per block were utilized in order to provide a good experimental error or noise assessment and to better estimate this variability. For this purpose, Design Expert 10.1 (StatEase, Minneapolis, MN, USA) and Statistica 13.5 (TIBCO Software, Palo Alto, CA, USA) software was utilized.

The extent of the removal of CIP was monitored by high performance liquid chromatography (HPLC) using an LC-20 series chromatograph equipped with an SPD-M20A UV/diode array diode detector (Shimadzu, Kyoto, Japan). An isocratic elution method was employed, using a mobile phase consisting of 80:20 aqueous solution of 0.1% v/v formic acid (VWR Chemicals, Lutterworth, UK): methanol (J.T. Baker, Radnor, PA, USA) and reverse-phase 150 mm × 4.6 mm, 5 μm, Atlantis T3 C18 column (Waters, Milford, MA, USA). CIP was monitored at a wavelength λ = 270 nm. An 0.5 mL aliquot was withdrawn from the photoreactor, filtered through a 0.45 μm syringe filter cartridge (Macherey-Nagel, Düren, Germany), and submitted for HPLC analysis. LabSolutions 5.97 SP1 (Shimadzu, Kyoto, Japan) software was used for HPLC data acquisition and analysis.

2.4. Characterization of the Photocatalysts

2.4.1. Identification of Crystalline Phases

The crystallinity and composition of the obtained photocatalysts was analyzed by powder X-ray diffraction (PXRD) using a MiniFlex 600 (Rigaku, Tokyo, Japan) equipped with a Cu Kα X-ray tube, a D/tex 1D silicon detector, and a sample spinner attachment. The X-ray tube was operated at a voltage of 40 kV and current of 10 mA. The samples were finely ground by hand using a pestle and mortar. XRD data acquisition and analysis was performed in SmartLab II studio v4.3.287.0 software (Rigaku, Tokyo, Japan). The data were recorded at a scan rate of 5 $^\circ$ min^{-1}, with a step size of 0.01° and 30 rpm sample stage rotation. The Crystallography Open Database (COD) 2020 was used to identify mineral phases.

2.4.2. Characterization of Surface Elemental Composition and Electronic States

The morphology of the gold-sputtered samples was investigated using an Ultra Plus field-emission scanning electron microscope (FE-SEM, Zeiss, Oberkochen, Germany) in addition to energy dispersive X-ray spectroscopy (EDS) characterization of the unsputtered samples in order to assess the surface composition. A 2 kV FE-SEM acceleration voltage was used. X-ray Photoelectron Spectroscopy (XPS) measurements on immobilized samples on FTO glass substrates were taken. In brief, fluorine-doped, tin-oxide-coated glass (FTO, Sigma Aldrich, St. Louis, MO, USA) was coated with a dispersion of the sample in silica/titanate sol-gel binder, as described previously in Section 2.3. The XPS characterization was performed using a VersaProbe III (Version AD) by PHI (Chanhassen, MN, USA) equipped with a hemispherical analyzer and a monochromatic Al Kα X-ray source. Survey spectra were measured using a pass energy of 224 eV and a step of 0.8 eV. Data were acquired using the ESCApe 1.4 software (Shimadzu-Kratos, Wharfside, Manchester, UK). The fitting of the core spectra was performed using CasaXPS 2.3 software (Casa Software Ltd., Teignmouth, UK).

2.4.3. Determination of Opto-Electronic Properties

Electrochemical characterization was performed according to our previous work [35]. A total of three layers were deposited onto an FTO substrate to prepare the working photoelectrodes. The coated FTO substrates were used as working electrodes in a typical-three electrode electrochemical setup, while a platinum (Pt) wire was used as a counter electrode, and a saturated calomel (SCE) reference electrode was utilized. An SP-150 potentiostat/galvanostat (Biologic, Seyssinet-Pariset, France) was used to perform the linear sweep

voltammetry (LSV) and electrochemical impedance spectroscopy (EIS) measurements. The electrochemical experiments were conducted in the dark and under illumination by a white light emitting diode (LED). The LSV measurements were performed at a scan rate of 20 mV s^{-1} from −0.5 V to +1.5 V vs. SCE. The EIS measurements were performed at 0 V vs. SCE at a frequency sweep from 100 kHz to 100 mHz using an AC amplitude of ±5 mV in relation to the open circuit potential. A 0.1 M solution of sodium chloride (0.1 M NaCl, 99%, Sigma-Aldrich, Waltham, MA, USA) was used as the electrolyte. The obtained EIS data were fitted to a model of an equivalent electrical circuit depicted in Figure S8 [36,37]. For this purpose, ZSimpWin 3.2 software was used (Ametek Scientific Instruments, Berwyn, PA, USA). Additionally, Mott–Schottky measurements were carried out to determine the Fermi level of the samples [35]. Open circuit potentials (OCPs) were measured by allowing the photoelectrodes to stabilize for 10 min, after which they were exposed to illumination for 10 min, after which the light source was turned off. The diffuse reflectance spectra (DRS) of immobilized samples on glass substrates was measured using a 2600i UV-Vis spectrophotometer equipped with an ISR-2600Plus integrating sphere (Shimadzu, Kyoto, Japan). The recorded spectra were plotted as Tauc plots using the Kubelka–Munk transformation [35].

3. Results and Discussion

3.1. Photocatalytic Effectiveness of Fe@BVO and Ag@BVO towards CIP Degradation

The aqueous solutions of CIP can undergo photolysis; thus, when considering photocatalytic degradation, the contribution of photolysis has to be taken into account. As shown in Figure S1, at pH 4, CIP is stable towards photolysis even after 240 min. At pH 6, the extent of photolysis is negligible, i.e., is less than 2%. Slightly alkaline conditions, on the other hand, favor photolysis. At pH 8, nearly 23% of CIP underwent photolytic degradation after 240 min. These results are in agreement with the findings of Torniainen et al. [38], whereby CIP was shown to be prone to photolysis in its zwitterionic form.

The activity of Fe@BVO and Ag@BVO for the degradation of CIP in photocatalytic experiments, according to the experimental plan in Table S2, and non-modified BVO as a reference are shown in Figure S2 (Supplementary Information). The contribution to the removal of CIP from the solution onto the immobilized films was established by measuring the extent of adsorption in the dark (shown in Figure S2 as the period from −30 to 0 min). At pH 4 and pH 6, the extent of adsorption is less than 8%; thus, the removal achieved during the photocatalytic experiments under illumination at these pH values corresponds to direct degradation of CIP. However, at pH 8, the extent of removal during the initial dark period is somewhat greater, with the greatest extent of adsorption being achieved by 50% Fe@BVO, which is equal to 16.1%.

The response surfaces, i.e., removal extents of CIP achieved in the investigated experiments, are shown in Figure 1. As observable by glancing at the results in Figure S2, the effect of Fe wt% content on the effectiveness of Fe@BVO is, at best, marginal, whereas the Ag loading on Ag@BVO had a marked effect. Moreover, the effectiveness of Ag@BVO at pH 4 for the removal of CIP is relatively unaffected by the wt% of Ag during the photomodification procedure (Figure S2A), unlike at pH 6 and pH 8. Furthermore, as can be seen, Ag loadings greater than 1% seemingly negatively affected the performance of the Ag@BVO photocatalyst. The Fe loading in Fe@BVO did not show a significant effect for the removal of CIP; moreover, with higher Fe loadings, the photocatalytic performance decreased. In the performed experiments, at pH 4 and pH 6, Fe@BVO achieved a removal of CIP that was within 5% of BVO alone in nearly all cases. However, at pH 8, 5% and 50% Fe@BVO achieved a markedly lower removal than BVO alone, i.e., 16.7% less CIP was removed with 5% Fe@BVO and 18.0% with 50% Fe@BVO (Figure S1). In order to ascertain the effects of the Fe- and Ag-modification of BVO, analysis of variance (ANOVA) of the gathered data provided further insights and helped elucidate the margins of experimental error.

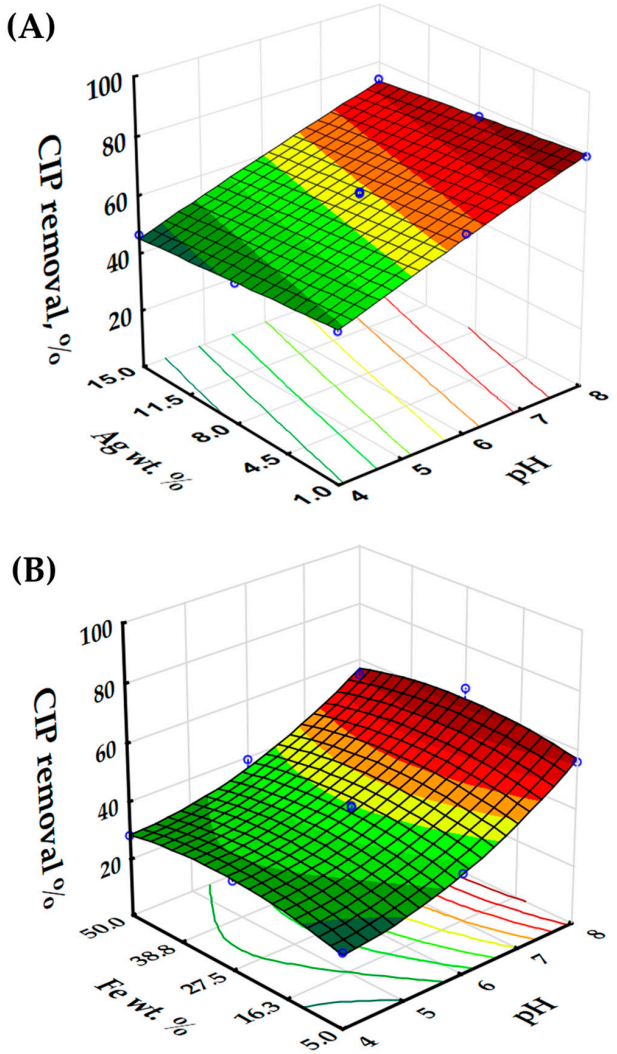

Figure 1. Response surface models for (**A**) the removal of CIP with the Fe@BVO photocatalyst and (**B**) with the Ag@BVO photocatalyst.

The obtained response surface models for the degradation of CIP by Fe@BVO and Ag@BVO are shown in Figure 1A,B, respectively. The response surface quadratic model equation for the removal of CIP by Fe@BVO (R_1) is shown in Equation (1):

$$R_1 = 41.22 + 15.26 \times X_1 + 0.96 \times X_2 - 0.95 \times X_1 \times X_2 + 5.70X_1^1 - 5.45X_2^2 \quad (1)$$

The *F*-value for the model equation R_1 describing the removal of CIP by the Fe@BVO process (Equation (1)) is 57.88, indicating that the model explains variance very well. In addition, the *p*-value of <0.0001 implies that the model is significant. Furthermore, the R^2 value is 0.9797, implying a good fit to the obtained data. The adjusted R^2, equal to 0.9957, which takes into account the number of variables in the model and their relevance, suggests that the independent variables contribute significantly to the predicted response. However, the only significant factors, from a standpoint of the *p*-value, in the model R_1 are X_1 ($p \leq 0.0001$) and ${X_1}^2$ ($p = 0.0036$). A summary of the analysis of variance is provided in Table S2, thus painting a somewhat contrasting picture and implying potential model overfitting. Despite the non-significance of the remainder of the parameters, these parameters contribute for the accounting of the additional variance in the removal model, mostly through non-linear relationships or small-magnitude interactions. The Pred-R^2 of 0.8252 implies that the model should generalize new data well, and the adequate precision ratio of 22.74 implies that the signal-to-noise ratio is very good. In other words, based

on the performed experiments, we can infer that the Fe loading in the photomodification procedure and/or pH in the Fe@BVO process have an intricate interplay that needs to be elucidated further, which is not immediately evident from Figure S2. The response model equation R_1 reveals that pH has, by far, the largest effect on the degradation of CIP, and that alkaline conditions are more favorable for CIP degradation, considering the positive weight of the factor X_1. This can only be partly attributed photolysis. The photocatalytic degradation experiments were carried out under illumination for 90 min; therefore, the extent of photolysis is small (Figure S1). It is likely that the Fe-photomodification facilitated improved photocatalytic activity in alkaline conditions.

On the other hand, the response surface quadratic model equation for the removal of CIP with the Ag@BVO process (R_2) is shown in Equation (2):

$$R_2 = 62.99 + 13.91 \times X_1 - 3.13 \times X_2 - 0.075 \times X_1 \times X_2 - 0.68X_1^1 - 0.056X_2^2 \quad (2)$$

The high F-value (102.58) and very small p-value (<0.0001) reveal that the model is statistically significant, i.e., that the model can explain a substantial amount of variance in the modeled response and to a larger extent than model R_1. The large R^2 value of 0.9884 and adjusted R^2 of 0.9788 suggest that the model explains a large proportion of the variance of the response. In addition, the predicted R^2 of 0.9186 is in good agreement with the adjusted R^2. Both X_1 and X_2 parameters are significant, with p values of <0.0001 and 0.0025, respectively. These p-values indicate that both pH and Ag wt% significantly impact the response, i.e., the removal extent of CIP in the Ag@BVO process. The interaction term $X_1 \times X_2$ has a p-value of 0.9258, implying that the interaction between pH and Ag wt% is not significant in explaining the variation in the removal extent of CIP, unlike in the case with Fe@BVO. The quadratic terms, i.e., ${X_1}^2$ and ${X_2}^2$, are equal to 0.5012 and 0.9549, implying that these terms are not significant for the response of the Ag@BVO model. Indeed, as can be seen from Figure 1B, the removal extent of CIP is linearly dependent on pH and Ag wt%. Considering the model equation, pH is the dominant contributing factor for the removal of CIP, whereas the Ag wt% has a negative impact, implying that lower silver loadings are more favorable. That is to be expected above a certain point, as photomodification with silver can block active sites of BVO and increase recombination rates [27].

In order to elucidate the effects of BVO modification on photocatalytic performance, the obtained materials were characterized in detail.

3.2. Characterization of the Fe@BVO and Ag@BVO Photocatalysts

Powder X-ray diffraction analysis revealed that the crystalline structure of the iso-type homojunctions is retained, and, in the case of the Ag modified samples, metallic silver has been identified as a phase present in the samples 8% Ag@BVO and 15% Ag@BVO, as shown in Figure 2 (for the sake of brevity, only the concentrations corresponding to highest X_2 coded-variables are shown). Interestingly, no iron species were identified, regardless of the instrumental parameters, i.e., slower scan rate and faster sample spinner settings. The identified phases, according to the Crystallography Open Database, correspond to the following entry cards: clinobisvanite (COD 9013437) and dreyerite (COD 9011741) in all cases, and, for the silver modified sample, correspond to metallic silver (COD 9013047). Thus, XRD has confirmed that the iso-type homojunction $BiVO_4$ is able to reduce Ag^+ species to metallic nanosilver particles, presumably on the {010} facets [39].

In pursuit of Fe within the Fe@BVO, we turned to SEM/EDS. A side-by-side comparison of the 27.5 wt% Fe and 8 wt% Ag modified BVO, i.e., the compositions corresponding to the middle-coded variables X_2 in the performed DoE runs, are shown in Figure 3. The morphology of the obtained materials can be described as globular aggregates roughly of ~1 μm of diameter, formed by fusion of smaller individual particles (micrographs for all of the samples are given in Figure S3). The observed morphology is consistent for the morphology of pristine BVO [23], which is to be expected considering that photomodification is a mild procedure. The photodeposited species are not observable immediately on the

surface of the $BiVO_4$ particles, which is unsurprising considering their small crystallite size evident from the reasonably broad peaks at Figure 2. In the case of Fe@BVO, interestingly, no iron species were detected in the EDS spectra, akin to XRD, as shown in Figure S4. In the case of Ag@BVO, the presence of Ag is notable on the X-ray energy dispersive spectra for samples prepared with 8 wt% and 15 wt% Ag, as shown in Figure S5; however, at 1% Ag, the characteristic Lα electron was not detected, again in agreement with XRD. Presumably, the intensity of the characteristic Ag Lα peaks is indistinguishable from the background in the case of 1 wt% Ag@BVO.

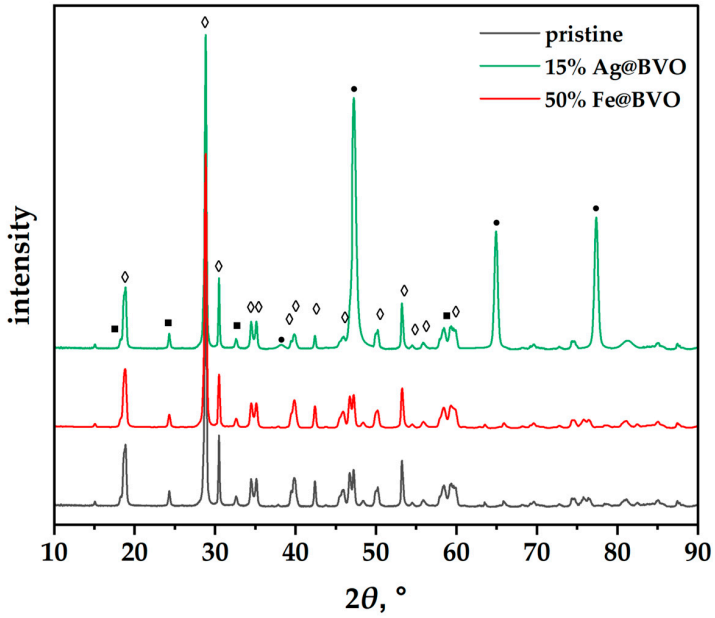

Figure 2. Powder X-ray diffractograms of pristine iso-type junction BVO, 50% Fe@BVO, and 15% Ag@BVO (peaks corresponding to phases: ◊—clinobisvanite, ■—dreyerite, ●—silver).

In order to further elucidate the properties of Fe@BVO and Ag@BVO samples, survey XPS spectra were recorded, as shown in Figure 4 (only the spectra for 50% Fe@BVO and 15% Ag@BVO are shown). The Ti $2p_{3/2}$ peak and Si 2p spectra originate from the silica/titanate coating used to immobilize $BiVO_4$ on FTO glass substrates for analysis, whereas C 1s implies leftover organics, most likely in the binder, owing to the low-temperature fixation procedure. In the context of $BiVO_4$, typical binding energies for O 1s are in the range of 531 eV to 532 eV, whereas, for Bi $4f_{5/2}$, the binding energies are 163 eV to 164 eV [40,41]. Again, no Fe species were identified, as was demonstrated previously by XRD and SEM/EDS, whereas, for Ag@BVO samples, the characteristic Ag 3d spectrum was observed in all cases. The observed O 1s spectra can be partly attributed to oxygen in the coating used to prepare the samples for XPS analysis and, to some extent, to oxygen within $BiVO_4$, as shown in Table 1. The bulk of the O 1s corresponds to OH^- groups [42]. The Bi $4f_{5/2}$ peak binding energies for 1% Ag@BVO and 5% Fe@BVO are relatively typical for pristine $BiVO_4$. However, the Bi $4f_{5/2}$ spectra for the 8% Ag@BVO and 27.5% Fe@BVO samples indicate that surface Bi^{3+} ions in the lattice have somewhat reduced oxidation states than would be expected. These reduced binding energies imply the formation of Bi–Bi bonds in the samples [43]. On the other hand, the greater binding energies for Bi $4f_{5/2}$ in the case of 15% Ag@BVO and 50% Fe@BVO imply a higher oxidation state relative to pristine $BiVO_4$. The peak position of the characteristic Ag 3d spectrum observed in Ag@BVO samples implies the presence of Ag^+ ions, i.e., the formation of surface oxidized silver species during photomodification [44]. The decrease in binding energy of Ag 3d with growing Ag content is to be expected, as the surface-formed silver oxides on the AgNPs interact with a larger bulk of silver nanoparticles, i.e., a greater initial concentration of Ag^+ precursor leads to the formation of somewhat larger AgNPs. This oxide appears to be limited to fringes of

the silver nanoparticles, as the only crystalline-silver-containing phase identified by XRD was metallic silver. Indeed, deconvoluted Ag 3d spectra shown in Figure S6 reveal that, with increasing Ag content during the photodeposition procedure, the overall oxidation state of Ag species decreases. In the case of 1% Ag@BVO, only AgO and Ag_2O species were detected. However, at the highest Ag loading, no characteristic peak for Ag_2O was detected, and the content of metallic Ag is greater than for 8% Ag@BVO. Thus, at higher Ag loadings, AgNPs are formed on the $BiVO_4$ surface, which are oxidized to a certain extent. The AgNPs are likely coated with the oxide layer, considering that the fringes of AgNPs are highly reactive [45].

Table 1. Characteristic spectra and corresponding XPS binding energies for Ag@BVO and Fe@BVO samples.

Spectra	Binding Energy in Sample, eV					
	1% Ag@BVO	8% Ag@BVO	15% Ag@BVO	5% Fe@BVO	27.5% Fe@BVO	50% Fe@BVO
O 1s	531.87	531.96	531.77	532.21	531.62	531.99
Bi $4f_{5/2}$	163.87	163.56	163.97	163.81	163.42	163.99
Ag 3d	367.27	367.16	366.97	-	-	-

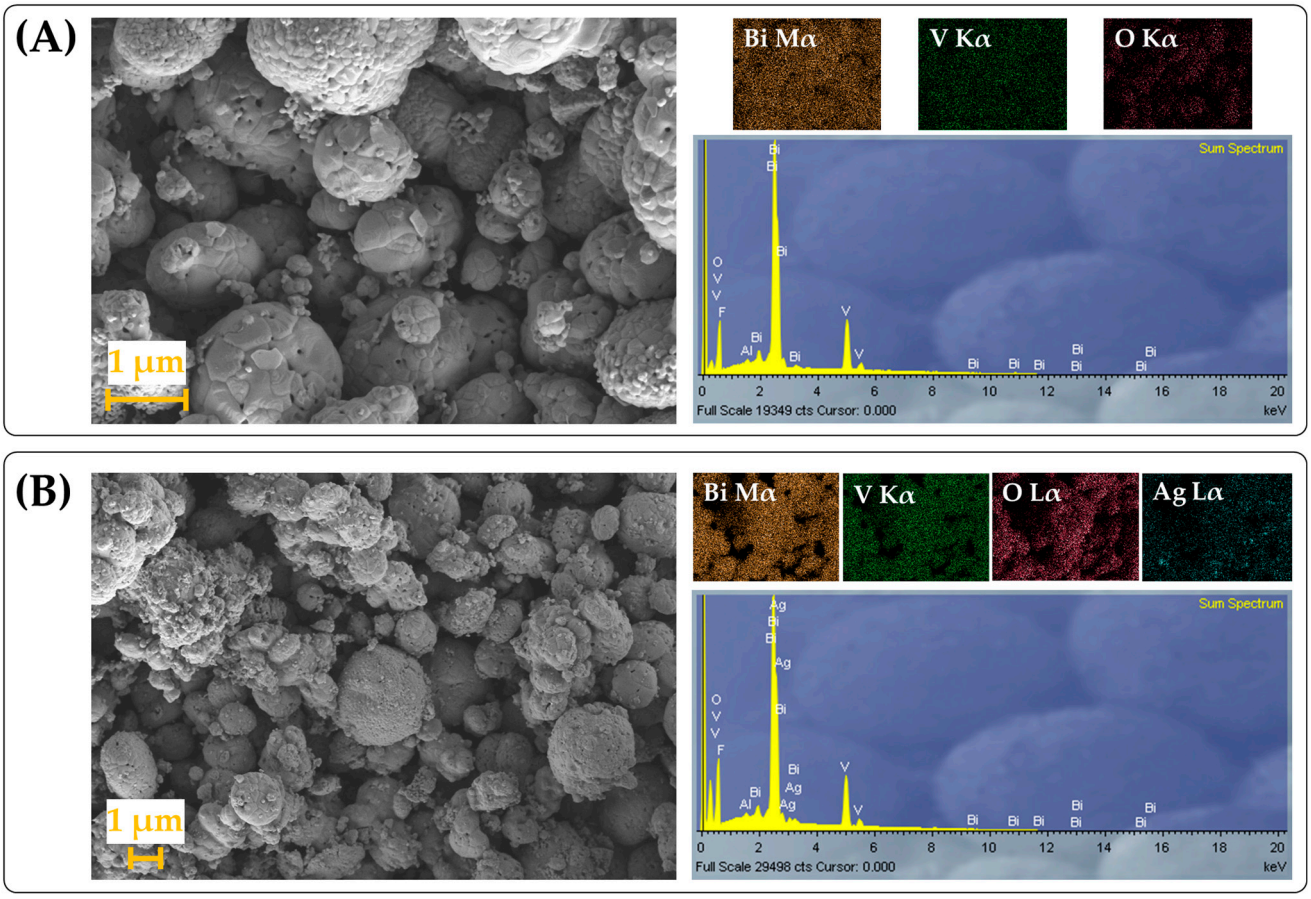

Figure 3. Morphology of the modified BVO materials by applied photomodification procedures and their corresponding energy dispersive X-ray spectra: (**A**) 27.5% wt. Fe@BVO, (**B**) 8% wt. Ag@BVO.

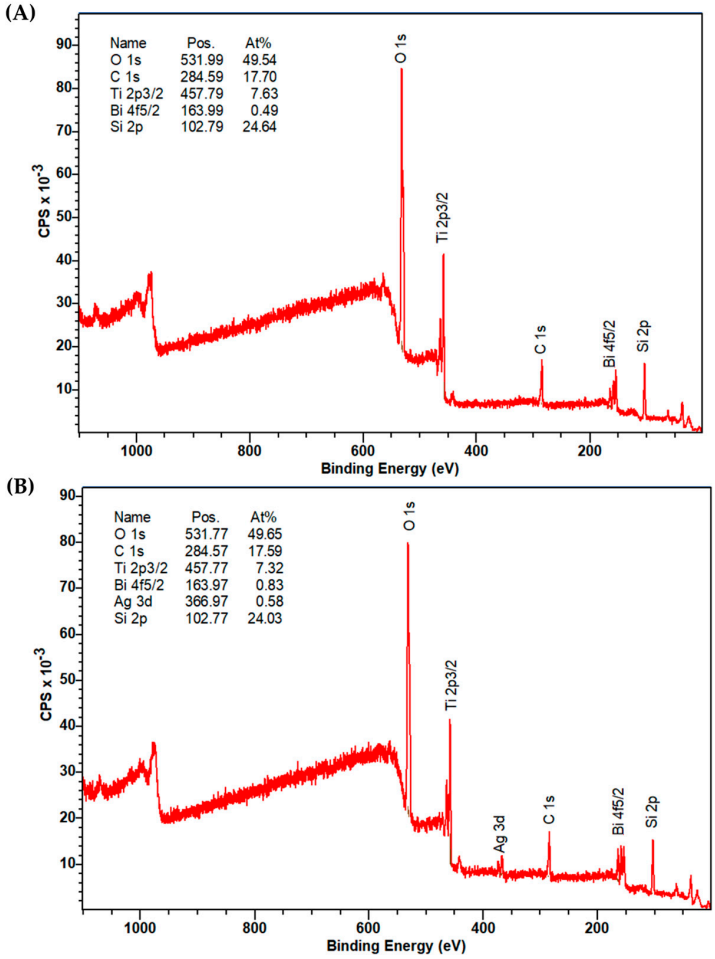

Figure 4. XPS survey spectra of (**A**) 50% Fe@BVO and (**B**) 15% Ag@BVO.

In general, smaller Ag nanoparticles (AgNPs) are more reactive than their larger counterparts and have a partial electron-donating character [46,47]. With lower Ag loading, it is likely that smaller nanoparticles are obtained, which are more susceptible to oxidation. In the case of Fe@BVO samples, an Fe concentration dependent behavior can be observed as well. Taking into consideration the standard reduction potentials of Fe^{2+} and Bi^{3+}, we can arrive at a hasty conclusion that reduction of Bi^{3+} with Fe^{2+} is unlikely ($Fe^{3+} + e^- \rightarrow Fe^{2+}$, $E^\circ = +0.770$ V; $Bi^{3+} + 3e^- \rightarrow Bi^0$, $E^\circ = +0.309$ V), which would be the case in the absence of light. However, during the attempted photomodification procedure, photogenerated holes accumulate on {110} facets of $BiVO_4$ [39]. The holes may oxidize Fe^{2+} to Fe^{3+}, thus forming surface oxygen vacancies by the reaction of Fe^{2+} with the Bi-O bond, thereby leading to a decreased Bi $4f_{5/2}$ splitting binding energy as detected by XPS. The scavenging of the photogenerated holes by Fe^{2+}, in turn, leads to an increased accumulation of photogenerated electrons on the {010} $BiVO_4$ facets [39], facilitating O_2 reduction to hydrogen peroxide [48]. Thus, favorable circumstances occur for the initiation of the photo-Fenton process during the photomodification procedure, whereby additional hydroxyl radicals (•OH) are generated. The •OH then, in turn, can fill oxygen vacancies formed in $BiVO_4$ formed by the aforementioned Fe^{2+} hole scavenging, thus leading to a greater Bi $4f_{5/2}$ binding energy for 50% Fe@BVO in relation to 27.5% Fe@BVO. The formation of oxygen vacancies can mediate the photogenerated charge recombination rates or facilitate electron mobility, into which electrochemical characterization will provide insights. In addition, oxygen vacancies are likely most stable in alkaline conditions [49], thus explaining the favorable effect of pH on the degradation of CIP with Fe@BVO observed in Figure 1B. Ab initio studies have shown that oxygen vacancies in the bulk of $BiVO_4$ trap electrons and thus may help hinder recombination, whereas those on the surface may facilitate charge

recombination [50]. Experimentalists have reported contrasting effects of oxygen vacancies on the electronic conductivity of $BiVO_4$ [51,52]; hence, further electrochemical characterization was deemed necessary to validate the hypothesis of the beneficial oxygen vacancy effect on Fe@BVO and to assess the effectiveness of Ag as an electron sink for Ag@BVO. In order to support this hypothesis, linear sweep voltammetry (LSV) and electrochemical impedance spectra (EIS) in the dark (D-) and under illumination (L-) were recorded. In addition, charge transfer resistances (R_{ct}) were determined by fitting the EIS data to an equivalent circuit model, as shown in Figure S8. The R_{ct} values are provided in Table S5. The equivalent circuit chosen uses a constant phase element (CPE) due to the heterogeneity of the photoelectrode surface [37].

The LSV in the case of Fe@BVO have so far confirmed the beneficial effect of the oxygen vacancies, as the photocurrent densities of the 27.5% and 50% Fe@BVO are improved over BVO alone, as shown in Figure 5A, stemming from the improved electron mobility. In the case of 5% Fe@BVO, a marginal improvement can be seen over BVO alone, owing to the lower density of oxygen vacancies. EIS has revealed that the charge carrier mobility, i.e., conductivity, has also increased in the case of the Fe@BVO in relation to pristine BVO, as shown in Figure 5C, as determined by the decreasing Nyquist semicircle radius. Thus, we can assert that the iso-type homojunction BVO benefits from surface oxygen vacancies, unlike monoclinic BVO alone [50]. The R_{ct} values for Fe@BVO, as shown in Table S5, have decreased in the dark in relation to BVO alone. The oxygen vacancies formed in the 5% and 27.5% Fe@BVO samples act as electron donors, thus enhancing the n-type behavior of BVO. In the case of 50% Fe@BVO, the notable changes in the Bi atom electronic environment and oxygen vacancies may have a synergistic role for electron transfer. Under illumination, the R_{ct} of Fe@BVO are less than half of BVO alone. In addition, the increasing Fe loading has had a positive impact on decreasing R_{ct}, although not to a great extent. However, the increased concentration of oxygen vacancies did not affect the band gap, i.e., the Fe@BVO samples exhibit a band gap energy similar to pristine BVO, as shown in Figure S7. In the case of Ag@BVO, we can see similar photocurrent densities regardless of the initial Ag wt% loading, as shown in Figure 5B. The anodic peaks at ~0.07 V vs. SCE correspond to the oxidation of AgNPs on the surface of $BiVO_4$. EIS has revealed similar charge carrier mobilities for 1% and 8% Ag, which are improved over BVO alone, whereas 15% Ag@BVO has markedly improved charge carrier mobility, as can be seen in Figure 5D, due to greatly enhanced photogenerated electron scavenging [53]. The measured charge transfer resistance for $BiVO_4$ on FTO electrode substrate in the dark is akin to the value reported in the literature by Chatchai et al. [54]. In the dark, 1% Ag@BVO demonstrated a significantly greater R_{ct} in relation to BVO alone, implying that silver oxide species impede charge transfer dynamics. At 8% Ag loading, the R_{ct} decreased, presumably due to the presence of metallic silver facilitating charge transfer. In the case of 15% Ag@BVO, R_{ct} is similar to BVO alone, presumably due to the formation of a Schottky barrier caused by a greater extent of band bending, and, hence, broadening the charge depletion region. However, under illumination, a stark decrease in R_{ct} is observed for all Ag@BVO samples, where a nearly five-fold reduction in charge transfer resistance is observed. The presence of AgNPs on the surface of Ag@BVO samples is notable from the weak surface plasmon resonance observed in the 2.0 to 2.2 eV range, whereas the band gap is marginally decreased by 0.04 eV, as shown in Figure S7. However, the improved photo-electrochemical properties of higher Ag content in the case of Ag@BVO are offset by the blockage of photocatalytic active sites, which leads to decreased effectiveness towards CIP degradation, as evidenced by the response surface model R_2 shown above. The flat band potential (E_{fb}) of the Fe and Ag modified BVO samples, determined by extrapolating the Mott–Schottky intercept with the x-axis in Figure S9, revealed a shift to more positive values. In particular, the flat band potential increased by 0.108 V for 50% Fe@BVO, whereas 15% Ag@BVO demonstrated a more positive shift by 0.219 V. Despite these shifts, the band gap remained largely the same. For Fe@VO, this hints at the formation of new quantum states within the band gap by oxygen vacancies. The oxygen vacancies lead to an absence of 2p orbitals in the conduction

band of BVO and thus cause a relative increase in the contribution of Bi cation orbitals in the valence band. Furthermore, these oxygen vacancies act as intermediate defects in the band gap, which facilitate electron transfer to the conduction band [55]. On the other hand, the positive shift of the flat band potential and the consecutive positive shift in the conduction band potential make Fe@BVO less likely to produce superoxide radicals, which are a major contributor to CIP degradation [56]. The faster shift of the open circuit potential after the photoelectrode is no longer illuminated towards a more positive potential, as shown in Figure S10A. This, in turn, implies that oxygen vacancies facilitate photogenerated charge recombination. These results are consistent with the findings made by Wang et al. [50]. In the case of Ag@BVO, the deposited AgNPs lead to the formation of a Schottky barrier. As the electrons migrate to the AgNPs, holes accumulate on the surface of the BVO, leading to the observed band bending effect and consequential flat band shift to more positive potentials [28]. The SPR of AgNPs on the surface of BVO contributes to the degradation of CIP by generating hot electrons, which facilitate reduction of oxygen to the superoxide radical [57]. While the Schottky barrier that forms at the AgNP/BVO interface could help photogenerated charge recombination, this effect is offset by the hot electrons generated by SPR that rapidly recombine with photogenerated holes. These electrons likely have sufficient energy to overcome the Schottky barrier and tend to rapidly recombine with holes, as can be seen in Figure S10B. The OCP shift towards the initial potential in the dark after termination of illumination is much faster than for Fe@BVO, implying faster charge recombination in Ag@BVO in relation to Fe@BVO and the iso-type homojunction BVO alone.

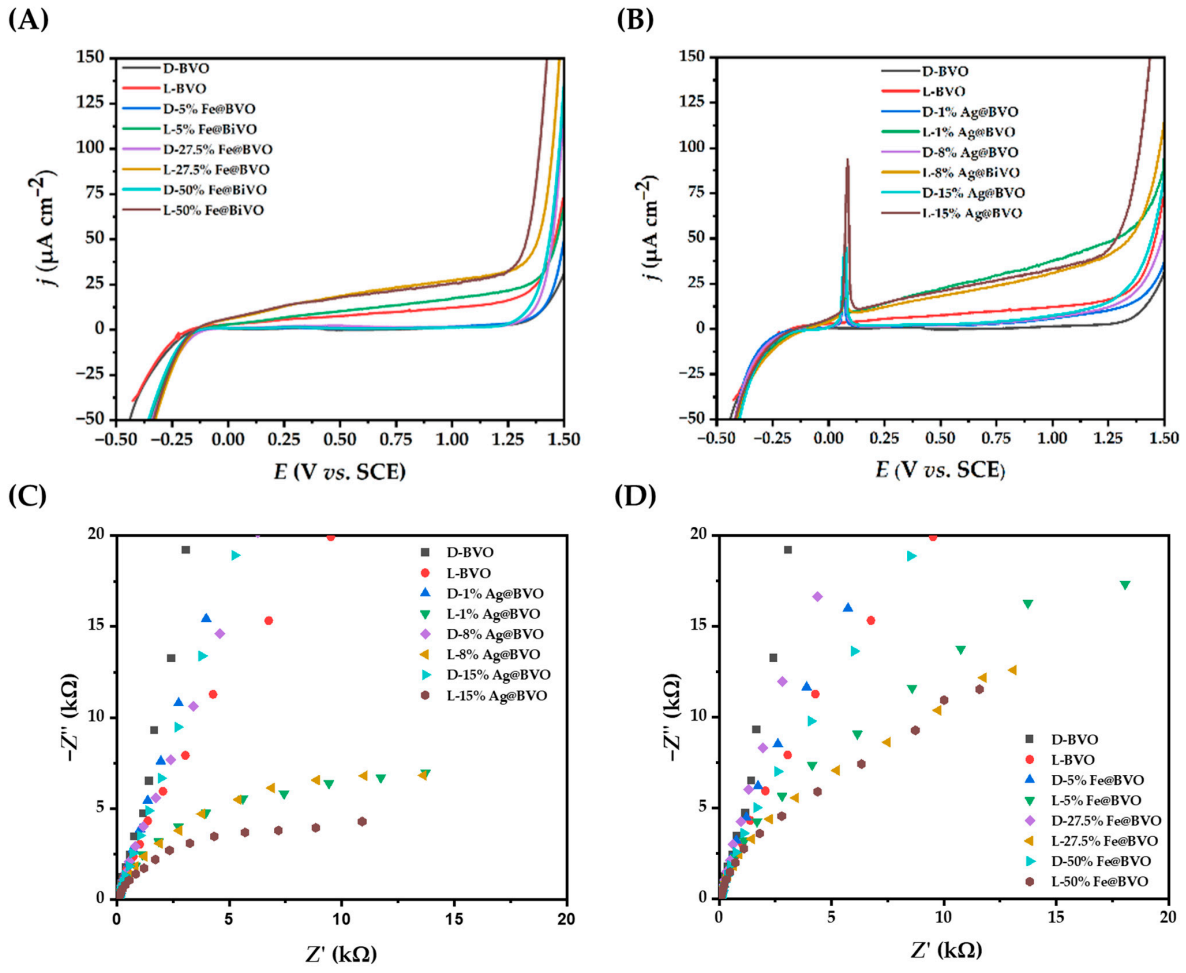

Figure 5. Linear sweep voltammograms for (**A**) Fe@BVO and pristine BVO in the dark (D-) and under illumination (L-); (**B**) Ag@BVO; (**C**) electrochemical impedance spectra for (**C**) Fe@BVO and (**D**) Ag@BVO.

4. Conclusions

The Fe photomodification on the pristine BVO iso-type homojunction lead to the formation of oxygen vacancies, as evidenced by XPS and Mott–Schottky analysis, which have facilitated improved electron mobility and increased the oxidative power of photogenerated holes. However, no Fe species whatsoever were detected in the samples. The concentration of oxygen vacancies is dependent on the mass ratio of pristine BVO in relation to the Fe^{2+} precursor, whereby the 27.5% mass fraction of the Fe^{2+} in relation to BVO during photodeposition resulted in a photocatalyst with improved degradation effectiveness for CIP in comparison to 5 and 50 wt% Fe. However, the impact of this improvement in the degradation of CIP was limited, as evidenced by the utilized response surface methodology stemming from the design of experiments approach. Considering the positive shift of the Fermi level of Fe@BVO, the formation of superoxide species, which contribute significantly to the degradation of CIP, is likely hindered. In addition, open circuit potential characterization has revealed that oxygen vacancies facilitate photogenerated charge recombination. Thus, the performance of Fe@BVO towards CIP degradation is comparable or worse than BVO alone, whereby, at pH 8, all of the Fe@BVO achieved markedly lower removals of CIP. Photomodification of BVO with the Ag(I) precursor resulted in the successful formation of AgNPs on the surface of Ag@BVO, whereby the photocatalytically most active sample is 1% Ag@BVO, despite the samples 8% and 15% Ag@BVO showing improved electronic properties. However, the improvement in the aforementioned properties is likely diminished by surface active site blocking by the AgNPs. Of the investigated photocatalysts, 1% Ag@BVO has achieved the highest removal effectiveness for CIP. The greater activity of Ag@BVO may be attributed to the better electron mobility by surface modification with AgNPs and to the generation of hot electrons by AgNP SPR, which facilitates superoxide generation. However, these hot electrons are also responsible for rapid photogenerated charge recombination. In terms of overall photocatalytic effectiveness, 1% Ag@BVO demonstrated highest activity for CIP degradation. At pH 4 and pH 6, 1% Ag@BVO achieved nearly 25% greater removal of CIP, whereas, at pH 8, the removal was only 6% greater.

Supplementary Materials: The following supporting information can be downloaded at: https://www.mdpi.com/article/10.3390/pr11092803/s1, Table S1: Full factorial design with coded variables (X) corresponding to experimental variables, i.e., pH and wt% of Fe^{2+} used during photomodification (Fe@BVO), and Ag^{+} wt% for Ag-modified $BiVO_4$ (Ag@BVO) investigated for the photocatalytic degradation of CIP; Table S2: Analysis of variance for the model for CIP removal using Fe@BVO under simulated solar irradiation; Table S3: Analysis of variance for the model for CIP removal using Ag@BVO under simulated solar irradiation; Table S4: Analysis of variance (ANOVA) of the model for the removal of CIP with Ag@BVO, and the analysis of variance for the model for CIP removal using Fe@BVO under simulated solar irradiation; Table S5: Charge transfer resistance (R_{ct}) obtained by fitting the measured EIS data to the model equivalent circuit shown in Figure S8; Figure S1: Extent of CIP photolysis under simulated solar irradiation at pH 4, pH 6, and pH 8; Figure S2: CIP remaining in solution during photocatalytic degradation (0 to 90 min) with BVO, Fe@BVO (5, 27.5, and 50 wt% Fe), and Ag@BVO (1%, 8%, 15% wt. Ag), including the initial removal in the dark (from −30 to 0 min) at (A) pH 4, (B) pH 6, and (C) pH 8; Figure S3: FE-SEM micrographs of Fe@BVO: (A) 5% wt. Ag, (B) 27.5% wt. Fe, (C) 50% wt. Fe; and Ag@BVO: (D) 1% wt. Ag, (E) 8% wt. Ag, (F) 15% wt. Ag; Figure S4: Energy dispersive X-ray (EDS) spectra of Fe@BVO samples, namely: (A) 5% wt. Fe, (B) 27.5% wt. Fe, (C) 50% wt. Fe content during photomodification; Figure S5: Energy dispersive X-ray spectra (EDS) of Ag@BVO samples, including sum spectra, for: (A) 1% wt. Ag, (B) 8% wt. Ag, (C) 15% wt. Ag loading on $BiVO_4$; Figure S6: Deconvoluted X-ray photoelectron spectra (XPS) of Ag@BVO samples: (A) 1% Ag@BVO, (B) 8% Ag@BVO, (C) 15% Ag@BVO; Figure S7: Diffuse reflectance spectra of (A) Fe@BVO and (B) Ag@BVO samples; Figure S8: Model equivalent circuit used to fit EIS data. R_s represents the solution resistance, R_{ct} charge transfer resistance, and Q_{dl} is a constant phase element related to the double layer capacitance; Figure S9: Mott–Schottky analysis of (A) 50% Fe@BVO and (B) 15% Ag@BVO; Figure S10: Open circuit potential (OCP) of (A) BVO and Fe@BVO photoelectrodes and (B) BVO and Ag@BVO photoelectrodes measured in the dark and under illumination.

Author Contributions: Conceptualization, T.S., H.K. and M.K.; methodology, T.S., M.P., M.K.R., B.G. and B.Ž.; formal analysis, M.K., B.G. and M.P.; investigation, M.P., T.S., M.K.R., B.G. and B.Ž.; resources, H.K., I.P., B.G. and U.L.Š.; data curation, M.P., T.S., B.G., B.Ž. and M.K.; writing—original draft preparation, M.K. and M.P.; visualization, M.K. and T.S.; supervision, H.K., A.L.B. and I.P.; project administration, H.K. and U.L.Š. All authors have read and agreed to the published version of the manuscript.

Funding: This research was funded by the Croatian Science Foundation, grant number IP-2018-01-1982 (Nano-sized Solar-active Catalysts for Environmental Technologies, NaSCEnT), the Croatian Government and the European Union through the European Regional Development Fund Operational Programme Competitiveness and Cohesion 2014-2020 through grants no. KK.01.1.1.04.0001 (Water Purification and Energy Conversion using Novel Composite Materials and Solar Irradiation) and KK.01.1.1.02.0005 (Atrium of Knowledge). In addition, this research was funded by the Multilateral Lead Agency bilateral agreement between the Slovenian Research Agency and Croatian Science Foundation, grant no. IPS-2022-02-4780 (Solar-assisted photocatalytic degradation of perfluorinated compounds in water, SoAPperF).

Data Availability Statement: The datasets collected and analyzed in this work are available from the corresponding authors upon reasonable written request.

Acknowledgments: We acknowledge the administrative and technical assistance provided by Nedjeljka Knežević of the University of Zagreb Faculty of Chemical Engineering and Technology.

Conflicts of Interest: The authors declare no conflict of interest.

References

1. Nguyen, T.D.; Nguyen, V.-H.; Nanda, S.; Vo, D.-V.N.; Nguyen, V.H.; Van Tran, T.; Nong, L.X.; Nguyen, T.T.; Bach, L.-G.; Abdullah, B.; et al. $BiVO_4$ photocatalysis design and applications to oxygen production and degradation of organic compounds: A review. *Environ. Chem. Lett.* **2020**, *18*, 1779–1801. [CrossRef]
2. Hooda, A.; Rawat, P.; Vaya, D. Insight into the Synthesis and Photocatalytic Applications of Bismuth Vanadate-based Nanocomposites. *Curr. Nanosci.* **2023**, *19*, 697–714. [CrossRef]
3. Monfort, O.; Plesch, G. Bismuth vanadate-based semiconductor photocatalysts: A short critical review on the efficiency and the mechanism of photodegradation of organic pollutants. *Environ. Sci. Pollut. Res.* **2018**, *25*, 19362–19379. [CrossRef]
4. Sudi, M.S.; Zhao, L.; Dou, Y.; Yang, X.; Wang, Q.; Wang, A.; Zhu, W. Enhanced photoelectrochemical water oxidation of a $BiVO_4$/tetra(amino)phthalocyanine composite photoanode. *J. Porphyr. Phthalocyanines* **2023**, *27*, 1434–1440. [CrossRef]
5. Xie, Z.; Chen, D.; Zhai, J.; Huang, Y.; Ji, H. Charge separation via synergy of homojunction and electrocatalyst in $BiVO_4$ for photoelectrochemical water splitting. *Appl. Catal. B Environ.* **2023**, *334*, 122865. [CrossRef]
6. Kalanur, S.S.; Jae Lee, Y.; Seo, H.; Pollet, B.G. Enhanced photoactivity towards bismuth vanadate water splitting through tantalum doping: An experimental and density functional theory study. *J. Colloid Interface Sci.* **2023**, *650*, 94–104. [CrossRef]
7. Song, S.; Xing, Z.; Zhao, H.; Li, Z. Recent advances in bismuth-based photocatalysts: Environment and energy applications. *Green Energy Environ.* **2023**, *8*, 1232–1264. [CrossRef]
8. Peng, X.; Liu, C.; Zhao, Z.; Hu, F.; Dai, H. Construction of a Z-scheme g-C_3N_4/NBGO/$BiVO_4$ heterostructure with visible-light driven photocatalytic degradation of tetracycline: Efficiency, reaction pathway and mechanism. *Catal. Sci. Technol.* **2022**, *12*, 1339–1358. [CrossRef]
9. Wang, Q.; Zhang, L.; Guo, Y.; Shen, M.; Wang, M.; Li, B.; Shi, J. Multifunctional 2D porous g-C_3N_4 nanosheets hybridized with 3D hierarchical TiO_2 microflowers for selective dye adsorption, antibiotic degradation and CO_2 reduction. *Chem. Eng. J.* **2020**, *396*, 125347. [CrossRef]
10. Liu, B.; Fang, Y.; Li, Z.; Xu, S. Visible-light nanostructured photocatalysts—A review. *J. Nanosci. Nanotechnol.* **2015**, *15*, 889–920. [CrossRef]
11. Zhou, W.; Xie, Q.; Lian, S. Photoelectrode materials for solar water splitting. *Prog. Chem.* **2013**, *25*, 1989–1998.
12. Fan, H.; Jiang, T.; Li, H.; Wang, D.; Wang, L.; Zhai, J.; He, D.; Wang, P.; Xie, T. Effect of $BiVO_4$ Crystalline Phases on the Photoinduced Carriers Behavior and Photocatalytic Activity. *J. Phys. Chem. C* **2012**, *116*, 2425–2430. [CrossRef]
13. Tokunaga, S.; Kato, H.; Kudo, A. Selective Preparation of Monoclinic and Tetragonal $BiVO_4$ with Scheelite Structure and Their Photocatalytic Properties. *Chem. Mater.* **2001**, *13*, 4624–4628. [CrossRef]
14. Kahraman, A.; Barzgar Vishlaghi, M.; Baylam, I.; Sennaroglu, A.; Kaya, S. Roles of Charge Carriers in the Excited State Dynamics of $BiVO_4$ Photoanodes. *J. Phys. Chem. C* **2019**, *123*, 28576–28583. [CrossRef]
15. Kodan, N.; Ahmad, M.; Mehta, B.R. Charge carrier separation and enhanced PEC properties of $BiVO_4$ based heterojunctions having ultrathin overlayers. *Int. J. Hydrogen Energy* **2021**, *46*, 189–196. [CrossRef]
16. Wang, X.; Liao, D.; Yu, H.; Yu, J. Highly efficient $BiVO_4$ single-crystal photocatalyst with selective Ag_2O-Ag modification: Orientation transport, rapid interfacial transfer and catalytic reaction. *Dalton Trans.* **2018**, *47*, 6370–6377. [CrossRef] [PubMed]

17. Aramugam, M.; Jagannathan, M.; Ashokkumar, M.; Arunachalam, P. A review on $BiVO_4$ photocatalyst: Activity enhancement methods for solar photocatalytic applications. *Appl. Catal. A Gen.* **2018**, *555*, 47–74.
18. Grushevskaya, S.; Belyanskaya, I.; Kozaderov, O. Approaches for Modifying Oxide-Semiconductor Materials to Increase the Efficiency of Photocatalytic Water Splitting. *Materials* **2022**, *15*, 4915. [CrossRef]
19. Yin, D.; Ning, X.; Zhang, Q.; Du, P.; Lu, X. Dual modification of $BiVO_4$ photoanode for synergistically boosting photoelectrochemical water splitting. *J. Colloid Interface Sci.* **2023**, *646*, 238–244. [CrossRef]
20. Wang, X.; Zhang, Y.; Deng, S.; Lin, S. Coupling surface modification with cocatalyst deposition on $BiVO_4$ photoanode to enhance charge transfer for efficient solar-driven water splitting. *Int. J. Hydrogen Energy* **2023**, *48*, 24320–24327. [CrossRef]
21. Li, S.; Li, Y.; Zhang, J.; Liu, X.; Zhang, K.; Zhang, Y.; Song, X.M. Charge separation at $BiVO_4/Co_3O_4$ and $BiVO_4$/CoOOH interfaces: Differences between dense and permeable cocatalysts. *Appl. Surf. Sci.* **2023**, *624*, 156965. [CrossRef]
22. Wenderich, K.; Mul, G. Methods, Mechanism, and Applications of Photodeposition in Photocatalysis: A Review. *Chem. Rev.* **2016**, *116*, 14587–14619. [CrossRef]
23. Sharifi, T.; Crmaric, D.; Kovacic, M.; Popovic, M.; Rokovic, M.K.; Kusic, H.; Jozić, D.; Ambrožić, G.; Kralj, D.; Kontrec, J.; et al. Tailored $BiVO_4$ for enhanced visible-light photocatalytic performance. *J. Environ. Chem. Eng.* **2021**, *9*, 106025. [CrossRef]
24. Sharifi, T.; Jozić, D.; Kovačić, M.; Kušić, H.; Lončarić Božić, A. In-situ high temperature XRD study on thermally induced phase changes of $BiVO_4$: The formation of an iso-type heterojunction. *Mater. Lett.* **2021**, *305*, 130816. [CrossRef]
25. Kohtani, S.; Hiro, J.; Yamamoto, N.; Kudo, A.; Tokumura, K.; Nakagaki, R. Adsorptive and photocatalytic properties of Ag-loaded $BiVO_4$ on the degradation of 4-n-alkylphenols under visible light irradiation. *Catal. Commun.* **2005**, *6*, 185–189. [CrossRef]
26. Li, J.; Zhou, J.; Hao, H.; Zhu, Z. Silver-modified specific (040) facet of $BiVO_4$ with enhanced photoelectrochemical performance. *Mater. Lett.* **2016**, *170*, 163–166. [CrossRef]
27. Wu, J.; Wang, Y.; Liu, Z.; Yan, Y.; Zhu, Z. Preparation of noble metal Ag-modified $BiVO_4$ nanosheets and a study on the degradation performance of tetracyclines. *New J. Chem.* **2020**, *44*, 13815–13823. [CrossRef]
28. Booshehri, A.Y.; Chun-Kiat Goh, S.; Hong, J.; Jiang, R.; Xu, R. Effect of depositing silver nanoparticles on $BiVO_4$ in enhancing visible light photocatalytic inactivation of bacteria in water. *J. Mater. Chem. A* **2014**, *2*, 6209–6217. [CrossRef]
29. Sánchez, O.A.; Rodríguez, J.L.; Barrera-Andrade, J.M.; Borja-Urby, R.; Valenzuela, M.A. High performance of Ag/$BiVO_4$ photocatalyst for 2,4-Dichlorophenoxyacetic acid degradation under visible light. *Appl. Catal. A Gen.* **2020**, *600*, 117625. [CrossRef]
30. Xu, X.; Du, M.; Chen, T.; Xiong, S.; Wu, T.; Zhao, D.; Fan, Z. New insights into Ag-doped $BiVO_4$ microspheres as visible light photocatalysts. *RSC Adv.* **2016**, *6*, 98788–98796. [CrossRef]
31. Ma, C.; Lee, J.; Kim, Y.; Cheol Seo, W.; Jung, H.; Yang, W. Rational design of α-Fe_2O_3 nanocubes supported $BiVO_4$ Z-scheme photocatalyst for photocatalytic degradation of antibiotic under visible light. *J. Colloid Interface Sci.* **2021**, *581*, 514–522. [CrossRef]
32. Oharisi, O.O.L.; Ncube, S.; Nyoni, H.; Madikizela, M.L.; Olowoyo, O.J.; Maseko, B.R. Occurrence and prevalence of antibiotics in wastewater treatment plants and effluent receiving rivers in South Africa using UHPLC-MS determination. *J. Environ. Manag.* **2023**, *345*, 118621. [CrossRef]
33. Zagui, G.S.; Moreira, N.C.; Santos, D.V.; Paschoalato, C.F.P.R.; Sierra, J.; Nadal, M.; Domingo, J.L.; Darini, A.L.C.; Andrade, L.N.; Segura-Muñoz, S.I. Multidrug-resistant Enterobacter spp. in wastewater and surface water: Molecular characterization of β-lactam resistance and metal tolerance genes. *Environ. Res.* **2023**, *233*, 116443. [CrossRef]
34. Kete, M.; Pavlica, E.; Fresno, F.; Bratina, G.; Štangar, U.L. Highly active photocatalytic coatings prepared by a low-temperature method. *Environ. Sci. Pollut. Res.* **2014**, *21*, 11238–11249. [CrossRef]
35. Sharifi, T.; Kovačić, M.; Belec, M.; Perović, K.; Popović, M.; Radić, G.; Žener, B.; Pulitika, A.; Kraljić Roković, M.; Lavrenčič Štangar, U.; et al. Effect of Functionalized Benzene Derivatives as Potential Hole Scavengers for BiVO4 and rGO-BiVO4 Photoelectrocatalytic Hydrogen Evolution. *Molecules* **2022**, *27*, 7806. [CrossRef]
36. Radić, G.; Perović, K.; Sharifi, T.; Kušić, H.; Kovačić, M.; Kraljić Roković, M. Electrochemical Characterisation of the Photoanode Containing TiO_2 and SnS_2 in the Presence of Various Pharmaceuticals. *Catalysts* **2023**, *13*, 909. [CrossRef]
37. Radić, G.; Šajnović, I.; Petrović, Ž.; Roković, M.K. Reduced graphene oxide/α-Fe_2O_3 fibres as active material for supercapacitor application. *Croat. Chem. Acta* **2018**, *91*, 481–490. [CrossRef]
38. Torniainen, K.; Tammilehto, S.; Ulvi, V. The effect of pH, buffer type and drug concentration on the photodegradation of ciprofloxacin. *Int. J. Pharm.* **1996**, *132*, 53–61. [CrossRef]
39. Hu, Y.; Gao, Y.; Liu, F.; Tian, Y.; Wang, Q.; Zeng, D.; Shen, T.; Song, J.; Guan, R.; Yuan, H. The {010} and {110} facets of $BiVO_4$ were selectively modified by Cu and g-C_3N_4 to enhance its visible light photocatalytic performance. *Sep. Purif. Technol.* **2023**, *323*, 124471. [CrossRef]
40. Talasila, G.; Sachdev, S.; Srivastva, U.; Saxena, D.; Ramakumar, S.S.V. Modified synthesis of $BiVO_4$ and effect of doping (Mo or W) on its photoelectrochemical performance for water splitting. *Energy Rep.* **2020**, *6*, 1963–1972. [CrossRef]
41. Tan, H.L.; Suyanto, A.; Denko, A.T.D.; Saputera, W.H.; Amal, R.; Osterloh, F.E.; Ng, Y.H. Enhancing the Photoactivity of Faceted $BiVO_4$ via Annealing in Oxygen-Deficient Condition. *Part. Part. Syst. Charact.* **2017**, *34*, 1600290. [CrossRef]
42. Dall'Antonia, L.H.; de Tacconi, N.R.; Chanmanee, W.; Timmaji, H.; Myung, N.; Rajeshwar, K. Electrosynthesis of Bismuth Vanadate Photoelectrodes. *Electrochem. Solid-State Lett.* **2010**, *13*, D29. [CrossRef]
43. Kim, J.; Duy, L.T.; Ahn, B.; Seo, H. Pre-oxidation effects on properties of bismuth telluride thermoelectric composites compacted by spark plasma sintering. *J. Asian Ceram. Soc.* **2020**, *8*, 211–221. [CrossRef]

44. Kim, S.H.; Choi, W.I.; Kim, K.H.; Yang, D.J.; Heo, S.; Yun, D.-J. Nanoscale Chemical and Electrical Stabilities of Graphene-covered Silver Nanowire Networks for Transparent Conducting Electrodes. *Sci. Rep.* **2016**, *6*, 33074. [CrossRef]
45. Sundaresan, V.; Monaghan, J.W.; Willets, K.A. Visualizing the Effect of Partial Oxide Formation on Single Silver Nanoparticle Electrodissolution. *J. Phys. Chem. C* **2018**, *122*, 3138–3145. [CrossRef]
46. Mallick, K.; Witcomb, M.; Scurrell, M. Silver nanoparticle catalysed redox reaction: An electron relay effect. *Mater. Chem. Phys.* **2006**, *97*, 283–287. [CrossRef]
47. Ivanišević, I.; Kovačić, M.; Zubak, M.; Ressler, A.; Krivačić, S.; Katančić, Z.; Gudan Pavlović, I.; Kassal, P. Amphiphilic Silver Nanoparticles for Inkjet-Printable Conductive Inks. *Nanomaterials* **2022**, *12*, 4252. [CrossRef]
48. Nikačević, P.; Hegner, F.S.; Galán-Mascarós, J.R.; López, N. Influence of Oxygen Vacancies and Surface Facets on Water Oxidation Selectivity toward Oxygen or Hydrogen Peroxide with $BiVO_4$. *ACS Catal.* **2021**, *11*, 13416–13422. [CrossRef]
49. Han, G.; Kim, J.Y.; Kim, K.-J.; Lee, H.; Kim, Y.-M. Controlling surface oxygen vacancies in Fe-doped TiO_2 anatase nanoparticles for superior photocatalytic activities. *Appl. Surf. Sci.* **2020**, *507*, 144916. [CrossRef]
50. Wang, W.; Strohbeen, P.J.; Lee, D.; Zhou, C.; Kawasaki, J.K.; Choi, K.-S.; Liu, M.; Galli, G. The Role of Surface Oxygen Vacancies in $BiVO_4$. *Chem. Mater.* **2020**, *32*, 2899–2909. [CrossRef]
51. Zhang, W.; Song, L.; Cen, J.; Liu, M. Mechanistic Insights into Defect-Assisted Carrier Transport in Bismuth Vanadate Photoanodes. *J. Phys. Chem. C* **2019**, *123*, 20730–20736. [CrossRef]
52. Qiu, W.; Xiao, S.; Ke, J.; Wang, Z.; Tang, S.; Zhang, K.; Qian, W.; Huang, Y.; Huang, D.; Tong, Y.; et al. Freeing the Polarons to Facilitate Charge Transport in $BiVO_4$ from Oxygen Vacancies with an Oxidative 2D Precursor. *Angew. Chem. Int. Ed.* **2019**, *58*, 19087–19095. [CrossRef]
53. Fan, H.; Yi, G.; Zhang, Z.; Zhang, X.; Li, P.; Zhang, C.; Chen, L.; Zhang, Y.; Sun, Q. Fabrication of Ag particles deposited $BiVO_4$ photoanode for significantly efficient visible-light driven photoelectrocatalytic degradation of β-naphthol. *J. Environ. Chem. Eng.* **2022**, *10*, 107221. [CrossRef]
54. Chatchai, P.; Kishioka, S.-y.; Murakami, Y.; Nosaka, A.Y.; Nosaka, Y. Enhanced photoelectrocatalytic activity of FTO/WO_3/$BiVO_4$ electrode modified with gold nanoparticles for water oxidation under visible light irradiation. *Electrochim. Acta* **2010**, *55*, 592–596. [CrossRef]
55. Sun, Y.; Li, G.; Sun, W.; Zhou, X. Research progress on the formation, detection methods and application in photocatalytic reduction of CO_2 of oxygen vacancy. *J. CO2 Util.* **2023**, *67*, 102344. [CrossRef]
56. Orimolade, B.O.; Zwane, B.N.; Koiki, B.A.; Tshwenya, L.; Peleyeju, G.M.; Mabuba, N.; Zhou, M.; Arotiba, O.A. Solar photoelectrocatalytic degradation of ciprofloxacin at a FTO/$BiVO_4$/MnO_2 anode: Kinetics, intermediate products and degradation pathway studies. *J. Environ. Chem. Eng.* **2020**, *8*, 103607. [CrossRef]
57. Carrasco, E.; Stockert, J.C.; Juarranz, Á.; Blázquez-Castro, A. Plasmonic Hot-Electron Reactive Oxygen Species Generation: Fundamentals for Redox Biology. *Front. Chem.* **2020**, *8*, 591325. [CrossRef] [PubMed]